Plasmon-phonon coupling between mid-infrared chiral metasurfaces and molecular vibrations

MD SHAMIM MAHMUD,[1] DANIEL ROSENMANN,[2] DAVID A. CZAPLEWSKI,[2] JIE GAO,[1,3] AND XIAODONG YANG[1,4]

[1]*Department of Mechanical and Aerospace Engineering, Missouri University of Science and Technology, Rolla, MO 65409, USA*
[2]*Center for Nanoscale Materials, Argonne National Laboratory, Argonne, IL 60439, USA*
[3]*gaojie@mst.edu*
[4]*yangxia@mst.edu*

Abstract: Plasmon-phonon coupling between metamaterials and molecular vibrations provides a new path for studying mid-infrared light-matter interactions and molecular detection. So far, the coupling between the plasmonic resonances of metamaterials and the phonon vibrational modes of molecules has been realized under linearly polarized light. Here, mid-infrared chiral plasmonic metasurfaces with high circular dichroism (CD) in absorption over 0.65 in the frequency range of 50 to 60 THz are demonstrated to strongly interact with the phonon vibrational resonance of polymethyl methacrylate (PMMA) molecules at 52 THz, under both left-handed and right-handed circularly polarized (LCP and RCP) light. The mode splitting features in the absorption spectra of the coupled metasurface-PMMA systems under both circular polarizations are studied in PMMA layers with different thicknesses. The relation between the mode splitting gap and the PMMA thickness is also revealed. The demonstrated results can be applied in areas of chiral molecular sensing, thermal emission, and thermal energy harvesting.

1. Introduction

Chirality is a universal property of matter that is frequently found in nature. Chiral materials present two enantiomeric forms which, as mirror images, cannot be superimposed on each other by simple rotation or translation. The chiroptical responses under LCP and RCP light, such as CD and optical activity, can be observed in various natural materials like amino acids, but the responses are very weak. However, chiral metamaterials and metasurfaces have been recently designed to exhibit strong chiroptical responses based on different types of asymmetric structures [1], such as two intersecting rectangles [2], double-bar patterns [3], gammadion patterns [4], eta-shaped patterns [5], twisted elliptical holes [6], binary-pattern structures [7], slanted nanoholes [8], and stepped nanoapertures [9,10].

One important application of plasmonic metasurfaces is molecular sensing [11], where the coupling phenomena take place between the plasmonic resonances of metasurfaces and the phonon vibrational modes of deposited molecules. The plasmon-phonon coupling strength between metasurfaces and molecules is highly dependent on the absorption and field confinement properties of the designed metasurface. The strong coupling strength can be obtained when the rate of coherent energy exchange between the plasmonic resonant mode and the molecules is higher than their individual decay rates [12,13]. Strong coupling has been realized with plasmonic metasurfaces by confining the electromagnetic field into deep subwavelength volume [14,15]. Plasmonic metasurfaces can serve as a powerful molecular sensing platform by coupling the enhanced resonant local near field to the vibrational fingerprint of molecules, providing a direct link to the molecular properties and chemical bonding information [16–20]. Previous studies have focused on the plasmon-phonon coupling between achiral plasmonic metasurfaces and molecular vibrations under linearly polarized light. However, research on the plasmon-phonon coupling

between chiral plasmonic metasurfaces and molecular vibrations under circularly polarized light for molecular detection is still missing.

In this work, we design and demonstrate a unique type of chiral plasmonic metasurfaces with high CD in absorption over 0.65 across the mid-infrared frequency range of 50 to 60 THz. The plasmon-phonon coupling between the plasmonic resonance of chiral metasurfaces and the phonon vibrational mode of PMMA molecules at 52 THz under both LCP and RCP incident light is further explored. The mode splitting features in the absorption spectra of the coupled metasurface-PMMA systems due to the plasmon-photon coupling under both circular polarizations are studied and analyzed by varying the plasmonic resonance of chiral metasurface as well as the PMMA layer thickness. Furthermore, the relation between the mode splitting gap of the plasmon-phonon coupling and the PMMA thickness is revealed. The demonstrated results provide new paths for various applications such as chiral molecular sensing, chiral imaging, circular-polarization thermal emission, and thermal energy harvesting. For example, the study of plasmon-phonon coupling between chiral metasurfaces and chiral molecules under circularly polarized light can be directly used for chiral molecule sensing and detection. The chirality detection of biomolecules using chiral metasurfaces have recently been reported based on the off-resonance excitations of chiral molecules in near-infrared frequency range [21,22], where the plasmonic resonance of chiral metasurface does not overlap with either the electronic or vibrational transitions of chiral molecules. However, our current work can be further extended to study the direct interaction between the superchiral near-fields of mid-infrared chiral metasurfaces and the phonon vibrational transitions of chiral molecules in order to advance the applications of chiral molecule sensing and detection.

2. Design of mid-infrared chiral metasurfaces

The mid-infrared chiral plasmonic metasurface is designed with a three-layer metal-dielectric-metal structure, consisting of the eye-shaped resonators etched in the top gold (Au) layer with a thickness of 65 nm, the middle alumina (Al_2O_3) spacer with a thickness of 250 nm, and the bottom gold mirror with a thickness of 200 nm, deposited on a silicon substrate. The Au layers are deposited using a Lesker PVD250 electron beam evaporator and the Al_2O_3 dielectric layer is deposited by reactive sputtering (Lesker CMS18 system). The designed unit cell in the enantiomeric form of Form A is illustrated in Figs. 1(a) and 1(b), which shows strong absorption to the incident RCP light. Since the two enantiomer forms of Form A and Form B have opposite chiroptical response under circular polarization, here only the chiral metasurface in Form A is presented. The vertical and horizontal periods of the unit cell are $p_x = 2.1$ μm and $p_y = 1.8$ μm, respectively. The eye-shaped resonator contains an inner Au elliptical pattern with the major and minor axes of $a = 1.6$ μm, $b = 0.3$ μm and the rotation angle of $\theta = 8°$, which is located within an outer elliptical cutout area with the major and minor axes of $a_1 = 2.2$ μm, $b_1 = 1.0$ μm. The designed chiral metasurfaces are then fabricated by using focused ion beam (FIB) milling (FEI Helios Nanolab 600, 30 kV, 28 pA) to etch the top Au layer into the eye-shaped resonator array. Figure 1(c) shows a scanning electron microscope (SEM) top view image of the fabricated chiral metasurface in Form A.

Numerical simulations are performed using the CST Studio Suite software to calculate the chiroptical responses of chiral metasurfaces under LCP and RCP excitation, where the permittivity of alumina is taken from the experimental data [23] and the permittivity of gold is taken from the Brendel-Bormann model [24]. Periodic boundary conditions are imposed in both x and y directions of the unit cell. Figure 1(d) shows the electric field $|E|$ distributions across the plane 35 nm below the upper surface of the top Au layer ($z = 480$ nm) and across the plane 50 nm underneath the upper surface of the Al_2O_3 spacer ($z = 400$ nm) under both LCP and RCP incident light for the chiral metasurface without the top PMMA layer at the plasmonic resonance of 60 THz. It shows that under RCP excitation, the incident circularly polarized light is well coupled
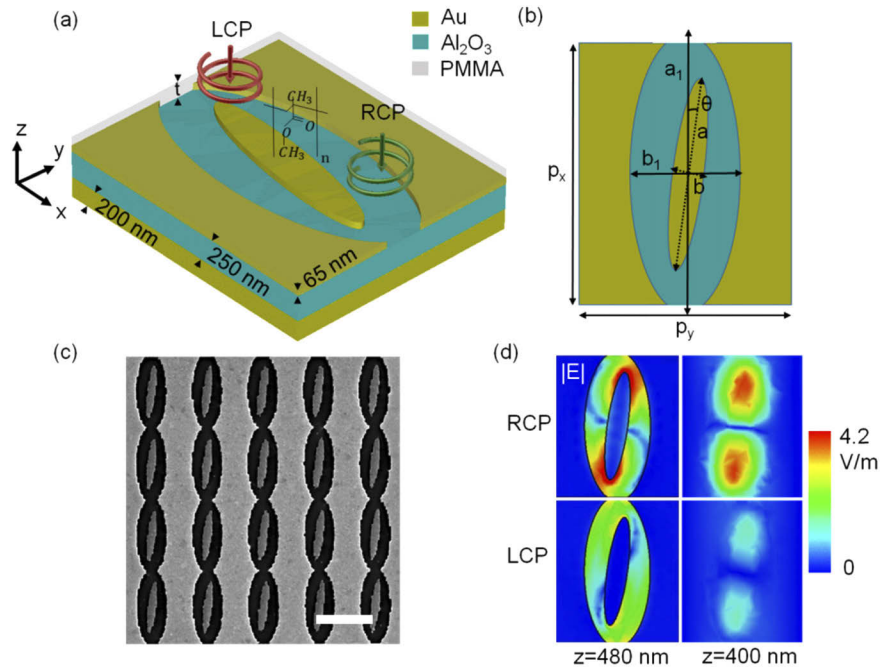
Fig. 1. (a) Schematic of the unit cell of the designed mid-infrared chiral plasmonic metasurface in Form A. (b) Top-view schematic of the unit cell with the designed geometric parameters. (c) SEM image of the fabricated chiral plasmonic metasurface in Form A. Scale bar: 2 μm. (d) Simulated electric field distributions in two z planes under LCP and RCP excitation at the plasmonic resonance of 60 THz.

into the eye-shaped resonators in Form A with the matched impedance, and the excited electric field from the dipole-like mode is strongly enhanced in the cutout area between the two ellipses and also inside the dielectric spacer, which leads to low reflection and strong absorption. One the other hand, under LCP excitation, only a small portion of the incident circularly polarized light is coupled into the eye-shaped resonators and most of the incident light gets reflected, so that the excited electric field of the dipole-like mode is weakly confined in the cutout area and the dielectric spacer, which results in low absorption. Therefore, the dipole-like mode localized along the major axis of the inner Au elliptical pattern under circularly polarized light contributes to the chiroptical response of the metasurface and enables the high CD in absorption. It is noted that the rotation angle and dimension of the inner elliptical pattern will affect the chiral field confinement and the trust region framework algorithm has been applied for determining the optimum structural configuration to maximize the chiroptical response and obtain the highest CD in absorption. The transmission is negligible ($T = 0$) due to the thick gold mirror layer, so the absorption is calculated by $A = 1 - R$, where A, T and R represent the absorption, transmission and reflection, respectively. The CD in absorption is defined as $CD = |A_{LCP} - A_{RCP}|$. With the optimum structural configuration shown in Fig. 1, the designed chiral metasurface in Form A exhibits chiral absorption around 0.89 under RCP light and a CD of around 0.71 at 60 THz in simulation.

In order to tune the plasmonic resonance across the desired mid-infrared frequency region of 50 to 60 THz, the geometric parameters g of p_x, p_y, a, b, a_1 and b_1 for each metasurface are scaled up by a factor of k^n as $g \cdot k^n$, with the scaling constant $k = 1.05$ and the exponent of $n = 0, 1, 2, 3, 4, 5$, while the rotation angle θ remains unchanged. A Fourier transform infrared

spectrometer (FTIR, Nicolet 6700) connected to an infrared microscope is used to measure the optical reflection spectra from the chiral metasurfaces, where the circular polarization of incident light is determined by using a linear polarizer and a quarter-wave plate. Figure 2 presents the measured and simulated absorption spectra of the chiral metasurfaces in Form A under LCP and RCP incidence. It shows that the chiral plasmonic resonance continuously decreases from 60 to 50 THz as the exponent of *n* increases from 0 to 5. The absorption for RCP incidence is much stronger than that for LCP incidence with the measured maximum chiral absorption over 0.93 and the measured CD in absorption of more than 0.65 across the frequency range of 50 to 60 THz.
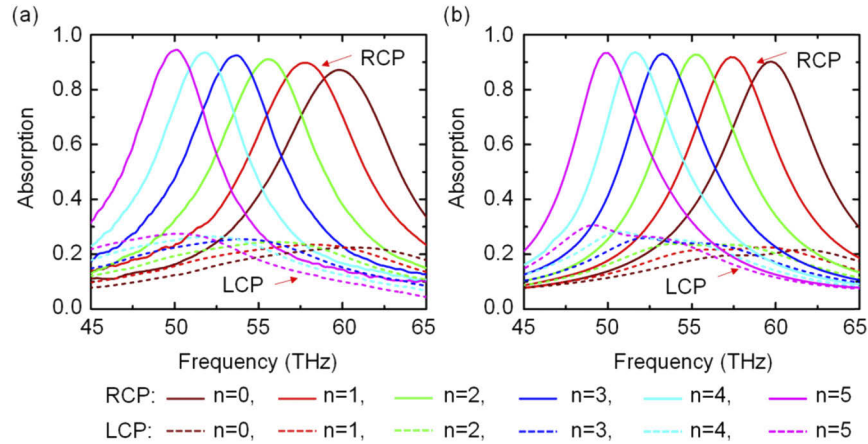

Fig. 2. (a) Measured and (b) simulated absorption spectra of the chiral metasurfaces in Form A with the scaled geometric parameters of $g \cdot k^n$, where $k = 1.05$ and $n = 0, 1, 2, 3, 4, 5$, under LCP and RCP incidence.

3. Plasmon-phonon coupling between chiral metasurfaces and PMMA molecules

Next, a thin PMMA layer is deposited on the top of the chiral metasurface of $n = 1$ at the plasmonic resonance of 57 THz for observing the plasmon-phonon interaction. The PMMA layer will introduce not only a phonon vibrational resonance but also create an increased permittivity immediately above the metasurface. In simulation, the permittivity of a PMMA layer is assumed to be constant with a value of $\varepsilon_b = 2.2$, without taking into account the phonon vibration mode. According to the simulation, due to the deposition of the PMMA layer, the plasmonic resonance of the chiral metasurface is redshifted from 57 THz to 52 THz. It is well known that the phonon vibrational resonance of the PMMA molecule C = O bond is located at the frequency of 52 THz, as shown in the previous studies [25,26]. The permittivity of an actual PMMA layer modeled using the Lorentz oscillator model of $\varepsilon_{PMMA} = \varepsilon_b - \varepsilon_L\omega_0^2/(\omega^2 - \omega_0^2 + i\omega\gamma_o)$ is then applied in simulation to obtain the plasmon-phonon coupling near the Lorentz resonance frequency of $\omega_0 = 3.269 \times 10^{14}$ rad/s (52 THz), with the background permittivity $\varepsilon_b = 2.2$, the Lorentz permittivity $\varepsilon_L = 0.018$, and the Lorentz damping rate $\gamma_o = 8.0 \times 10^{11}$ rad/s [18,19]. In experiment, three different thin layers of PMMA molecules dissolved into anisole (950A-2, Microchem) are spin coated on top of the fabricated metasurface. The thicknesses of the deposited PMMA layers measured using the FIB cross section and X-ray reflectivity (Philips X-Pert MRD) are $t = 80$, 140 and 200 nm.

Figure 3(a) plots the measured and simulated absorption spectra of the coupled metasurface-PMMA systems for the metasurface of $n = 1$ coated with the PMMA layers of three different thicknesses. For RCP excitation, the plasmonic resonance of the metasurface strongly interacts with the phonon vibrational resonance of PMMA molecules in the enhanced near field, resulting
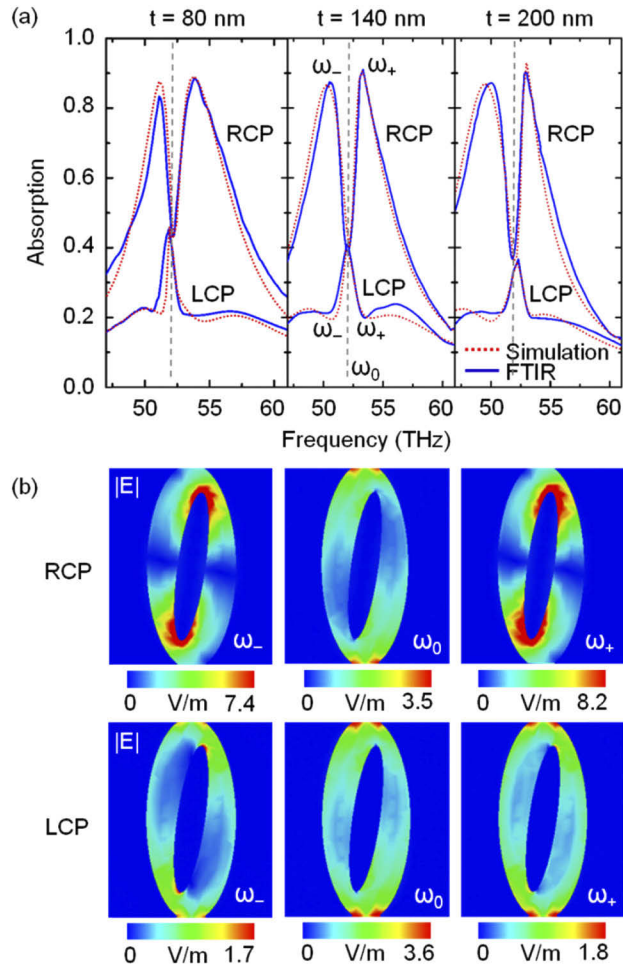
Fig. 3. (a) Measured and simulated absorption spectra of the coupled metasurface-PMMA systems with the PMMA thicknesses of $t = 80$, 140 and 200 nm. (b) Simulated electric field distributions across the plane of $z = 480$ nm under both LCP and RCP incidence at the frequencies of ω_-, ω_0 and ω_+ for the chiral metasurface coated with the 140 nm-thick PMMA layer.

in two coupled plasmon-phonon modes ($\omega_\pm$) featured as the dual absorption peaks around the frequency of $\omega_0 = 52$ THz, which are observed for all the three cases in both experiment and simulation. The absorption spectra exhibit the electromagnetically induced transparency (EIT)-like features with a minimum-absorption window around ω_0 between the two coupled plasmon-phonon modes with a mode splitting gap of $\delta = \omega_+ - \omega_-$, which arises from the destructive interference in the plasmon-phonon system. It is observed that the absorption at ω_0 diminishes as the PMMA thickness increases, indicating the stronger plasmon-phonon coupling strength which also corresponds to a larger mode splitting gap between the two plasmon-phonon eigenmodes. The measurement and simulation show a good agreement in all three cases. On the other hand, for the LCP excitation, the interaction between the weak plasmonic near field of the metasurface and the phonon vibrational resonance leads to almost the opposite features with the dual local absorption dips as the two coupled plasmon-phonon modes ($\omega_\pm$) around the absorption peak at ω_0. Such electromagnetically induced absorption (EIA)-like features

with a maximum-absorption window is a consequence of the constructive interference in the plasmon-phonon system. It shows that the absorption at ω_0 also diminishes and the mode splitting gap increases as the PMMA layer thickness increases, arising from the stronger plasmon-phonon coupling strength. The origin of the destructive interference and constructive interference in the plasmon-phonon system can be further explained by the coupling analysis [27,28]. Under the excitation of circularly polarized light, part of the incident light is coupled into the plasmonic mode, while the rest uncoupled light is reflected back. The reflection of the plasmon-phonon system can be calculated by the loss ratio x between the coupling loss of incident light and the intrinsic loss of plasmonic resonance. The reflection from the plasmon-phonon system depends on the two amplitudes of the light coupled back from the plasmon-phonon system and the initially uncoupled light, which interfere destructively due to the phase difference of π between them. At critical coupling ($x = 1$), the two amplitudes are equal to each other so there is no reflection and the absorption reaches the maximum value of 1. For RCP excitation, the plasmonic mode is undercoupled ($x < 1$), and its interaction with phonon vibrational mode will drive the system far away from the critical coupling over the phonon resonance width. The light coupled back from the plasmon-phonon system is out of phase with the initially uncoupled light, and their destructive interference results in an increased reflection and a decreased absorption showing the EIT-like features. For LCP excitation, the plasmonic mode is overcoupled ($x > 1$), and the additional loss from the phonon vibrational mode will drive the system close to the critical coupling. The light coupled back is in phase with the uncoupled light, and their constructive interference gives an increased absorption showing the EIA-like features. Figure 3(b) displays the simulated electric field distributions across the plane of $z = 480$ nm under both LCP and RCP incidence at the frequencies of ω_-, ω_0 and ω_+ for the chiral metasurface coated with the 140 nm-thick PMMA layer. For RCP excitation at ω_0, the plasmonic near field is spread out inside the cutout region which increases the interaction volume between the plasmonic near field and the PMMA molecules around the cutout region, giving the destructive EIT-like mode with a low absorption. However, for the two coupled plasmon-phonon modes at ω_- and ω_+, the confined plasmonic near field is more localized around the inner gold ellipse and has much stronger intensity so that a high absorption is obtained. For LCP excitation at ω_0, the plasmonic near field is also spread out in the cutout region to interact with the PMMA molecules, showing the constructive EIA-like mode with a highly increased absorption. In contrast, the two coupled plasmon-phonon modes at ω_- and ω_+ exhibit weakly confined plasmonic near field and have much lower intensity which result in a low absorption.

   In order to further analyze the mode splitting behavior induced by the plasmon-photon coupling, twenty-four metasurface samples with different scaled geometric parameters are fabricated, where the plasmonic resonances of the bare metasurfaces without the top PMMA layer ω_b range from 48 to 67 THz, which allows the sweep of the plasmonic resonance redshifted by the PMMA layer across the phonon vibrational frequency ω_0. Figure 4(a) shows the measured and simulated absorption spectra under RCP incidence for the coupled metasurface-PMMA systems as a function of the plasmonic resonance ω_b with the PMMA thickness of $t = 80$, 140 and 200 nm, respectively. The anti-crossing behavior of two plasmon-phonon eigenmode branches is clearly observed for each case which results in a mode splitting gap, arising from the strong coupling between the plasmonic resonances and the phonon vibrational modes. When the plasmonic resonance is far away from the phonon vibrational mode, the plasmon-phonon interaction results in a Fano-like resonance [29,30]. But as the plasmonic resonance matches that of the phonon vibrational mode, EIT-like resonance is observed with the two new hybrid plasmon-phonon modes at ω_- and ω_+ and the mode splitting gap δ at ω_0. It is noted that the full-width at half-maximum (FWHM) of the plasmonic resonance ζ_{plasmon} and the phonon vibrational mode ζ_{phonon} satisfy the condition of $\delta > (\zeta_{\text{plasmon}} + \zeta_{\text{phonon}})/2$, which is the criteria of Rabi splitting [13,31,32]. It shows a good agreement between the simulated and measured absorption spectra. The observed mode splitting

gap δ gets larger from 2.90 THz to 3.29 THz and 3.54 THz as the PMMA thickness is increased from 80 nm to 140 nm and 200 nm. The experimentally measured FWHM of $\zeta_{plasmon}$ is 5.30 THz and the measured FWHM of ζ_{phonon} is 0.34 THz so that $(\zeta_{plasmon} + \zeta_{phonon})/2$ is 2.82 THz. It clearly shows that the criteria of Rabi splitting for strong coupling is satisfied for different PMMA thicknesses. The mode splitting gap increases with the coupling strength between the plasmonic resonances and the phonon vibrational modes [33–35], so that the coupling strength can be adjusted by altering the PMMA thickness. On the other hand, the absorption spectra under LCP incidence for the coupled metasurface-PMMA systems are plotted in Fig. 4(b), where the EIA-like resonance at ω_0 with high absorption is always predominant. Although the plasmon-phonon coupling is weak, the mode splitting features can still be observed with two dark branches having a relatively low absorption around ω_0, representing the two weakly coupled plasmon-phonon modes at ω_- and ω_+. The mode splitting gap δ also becomes larger from 2.44 THz to 2.71 THz and 3.02 THz as the PMMA thickness is increased from 80 nm to 140 and 200 nm. However, the mode splitting gaps for the RCP case are much larger than those in the LCP case, indicating the higher coupling strength present for RCP illumination, which agrees with the more concentrated plasmonic field in the cutout region at ω_0 shown in Fig. 3(b).
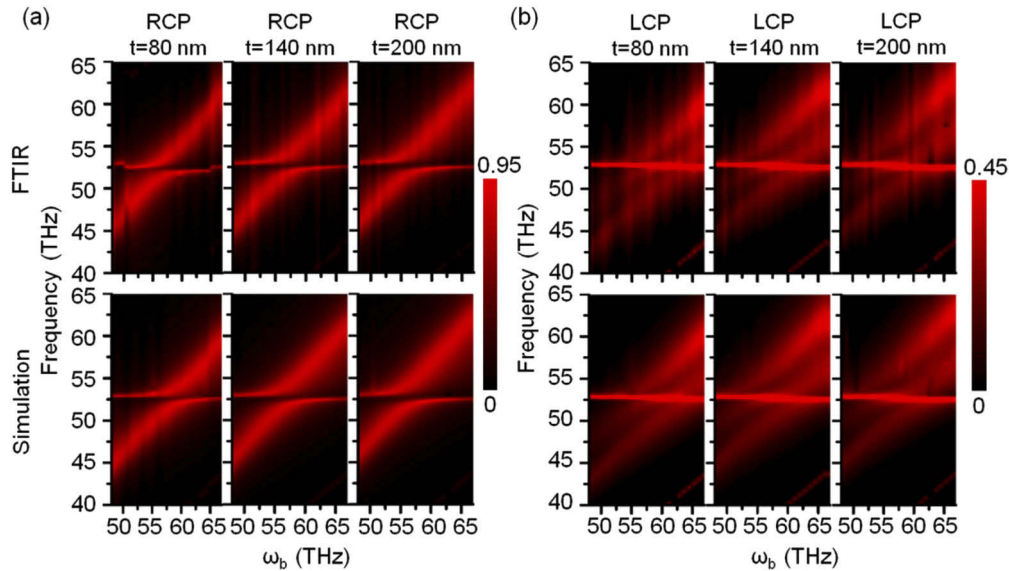

Fig. 4. Measured and simulated absorption spectra for the coupled metasurface-PMMA systems as a function of the plasmonic resonance ω_b under (a) RCP and (b) LCP incidence.

The relation between the coupling strength and the PMMA thickness can be further analyzed by checking the overlapped volume between the confined plasmonic resonant field and the PMMA molecules. Only the strong plasmon-phonon coupling under the RCP excitation is considered, due to the weak coupling in the LCP case. Figure 5(a) shows the simulated electric field distribution of the coupled metasurface-PMMA system with the PMMA thickness of 140 nm under RCP excitation at the phonon vibrational frequency of 52 THz in the cross section of $x = 10$ nm. It shows that the electric field is confined around the metasurface and decays exponentially into both the PMMA layer and the Al_2O_3 spacer. The electric field profiles along the white dashed line for different PMMA thicknesses are plotted in Fig. 5(b), indicating that the overlapped volume increases with the PMMA thickness. The total overlapped optical power between the plasmonic resonant field and the PMMA layer of thickness t can be expressed as $p_{tot} \propto \int_0^t E_0^2 e^{-2\sigma z} dz$, with the electric field $E = E_0 e^{-\sigma z}$ where E_0 is the electric field at the metasurface-PMMA interface and

σ is the decay rate. As the coupling strength depends on the amount of p_{tot}, the mode splitting gap δ is proportional to p_{tot} as a function of the PMMA thickness with $\delta = C\left(1 - e^{-2\sigma t}\right) + C_0$, where C and C_0 are two fitting parameters. C_0 represents the mode splitting gap when the PMMA molecules are only filled inside the cutout region. The mode splitting gap as a function of the PMMA thickness from 80 to 600 nm is simulated in Fig. 5(c). The fitting curve of δ is also plotted with the fitting parameters of $C = 2.32$ THz, $C_0 = 2.26$ THz, $\sigma = 2.07$ μm^{-1}, which shows a good agreement between the simulated and measured data. Since the electric field decays exponentially inside the PMMA layer, the plasmon-phonon coupling is strong near the metasurface-PMMA interface and becomes weaker away from the interface. The decay length of the electric field above the gold metasurface is approximately 350 nm which is calculated from

$l_d = \frac{\lambda}{2\pi}\left(\frac{-n^4}{\varepsilon'+n^4}\right)^{-\frac{1}{2}}$ [36,37], where ε' is the real part of the gold permittivity and n is the refractive index of PMMA. When the PMMA thickness t is within the decay range of l_d, the coupling strength increases with larger mode splitting gap as the PMMA layer gets thicker. For the PMMA molecules located above the decay length l_d, the coupling strength gets very weak so that the mode splitting gap becomes saturated around 4.58 THz. It indicates that the plasmon-photon coupling strength can be tuned effectively by varying the PMMA thickness. It is expected that the observed mode splitting behavior can be potentially used to characterize the molecule layer thickness and measure the plasmon-phonon coupling strength.
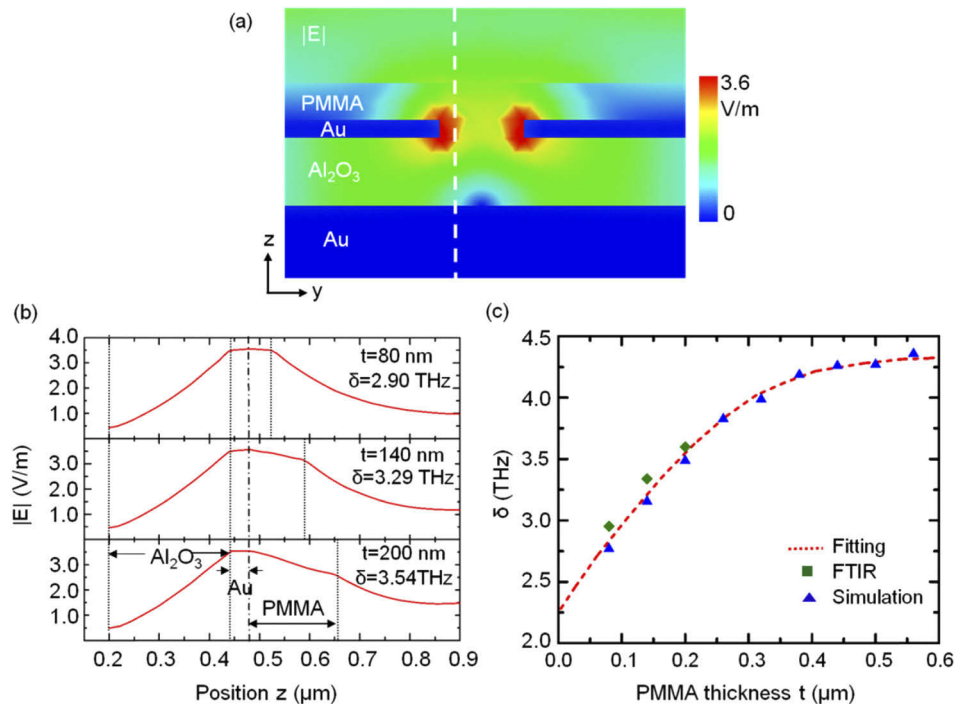

Fig. 5. (a) Electric field distribution of the coupled metasurface-PMMA system under RCP excitation at the cross section of $x = 10$ nm. (b) The electric field profiles along the white dashed line for PMMA thicknesses of 80, 140 and 200 nm. (c) The comparison of mode splitting gap between the fitting curve, the simulated result, and the FTIR measured data as the function of PMMA thickness.

4. Conclusion

In summary, we have designed and demonstrated the mid-infrared chiral plasmonic metasurfaces with high CD in absorption. The plasmon-phonon coupling between the plasmonic resonance of chiral metasurface and the phonon vibrational mode of PMMA molecules under both LCP and RCP excitation has been studied. The mode splitting features in the absorption spectra of the coupled metasurface-PMMA systems under both circular polarizations are studied. The anti-crossing behavior and the EIT-like resonance are observed for the RCP excitation due to the strong plasmon-phonon coupling, while the EIA-like resonance is obtained for the LCP case with the weak coupling. It is also demonstrated that the mode splitting gap can be tuned by varying the PMMA thickness within the decay length of the electric field. The demonstrated plasmon-phonon coupling phenomena with mid-infrared chiral metasurfaces depending on the incident circularly polarized light will open further opportunities for many applications such as ultrasensitive detection of chiral molecules, chiral imaging, circularly polarized thermal radiation, and thermal energy harvesting.

Disclosures

The authors declare no conflicts of interest.

References

1. J. T. Collins, C. Kuppe, D. C. Hooper, C. Sibilia, M. Centini, and V. K. Valev, "Chirality and Chiroptical Effects in Metal Nanostructures: Fundamentals and Current Trends," Adv. Opt. Mater. **5**(16), 1700182 (2017).
2. L. Kang, S. P. Rodrigues, M. Taghinejad, S. Lan, K.-T. Lee, Y. Liu, D. H. Werner, A. Urbas, and W. Cai, "Preserving Spin States upon Reflection: Linear and Nonlinear Responses of a Chiral Meta-Mirror," Nano Lett. **17**(11), 7102–7109 (2017).
3. L. Ouyang, W. Wang, D. Rosenmann, D. A. Czaplewski, J. Gao, and X. Yang, "Near-infrared chiral plasmonic metasurface absorbers," Opt. Express **26**(24), 31484–31489 (2018).
4. D.-H. Kwon, P. L. Werner, and D. H. Werner, "Optical planar chiral metamaterial designs for strong circular dichroism and polarization rotation," Opt. Express **16**(16), 11802–11807 (2008).
5. B. Tang, Z. Li, E. Palacios, Z. Liu, S. Butun, and K. Aydin, "Chiral-Selective Plasmonic Metasurface Absorbers Operating at Visible Frequencies," IEEE Photonics Technol. Lett. **29**(3), 295–298 (2017).
6. S. Wang, L. Kang, and D. H. Werner, "Active Terahertz Chiral Metamaterials Based on Phase Transition of Vanadium Dioxide (VO2)," Sci. Rep. **8**(1), 189 (2018).
7. Z. Li, D. Rosenmann, D. A. Czaplewski, X. Yang, and J. Gao, "Strong circular dichroism in chiral plasmonic metasurfaces optimized by micro-genetic algorithm," Opt. Express **27**(20), 28313–28323 (2019).
8. Y. Chen, J. Gao, and X. Yang, "Chiral Metamaterials of Plasmonic Slanted Nanoapertures with Symmetry Breaking," Nano Lett. **18**(1), 520–527 (2018).
9. Y. Chen, J. Gao, and X. Yang, "Chiral Grayscale Imaging with Plasmonic Metasurfaces of Stepped Nanoapertures," Adv. Opt. Mater. **7**(6), 1801467 (2019).
10. Y. Chen, X. Yang, and J. Gao, "3D Janus plasmonic helical nanoapertures for polarization-encrypted data storage," Light: Sci. Appl. **8**(1), 45 (2019).
11. A. Ben-Moshe, B. M. Maoz, A. O. Govorov, and G. Markovich, "Chirality and chiroptical effects in inorganic nanocrystal systems with plasmon and exciton resonances," Chem. Soc. Rev. **42**(16), 7028–7041 (2013).

12. D. S. Dovzhenko, S. V. Ryabchuk, Y. P. Rakovich, and I. R. Nabiev, "Light-matter interaction in the strong coupling regime: configurations, conditions, and applications," Nanoscale **10**(8), 3589–3605 (2018).
13. P. Torma and W. L. Barnes, "Strong coupling between surface plasmon polaritons and emitters: a review," Rep. Prog. Phys. **78**(1), 013901 (2015).
14. S. Campione, A. Benz, J. F. Klem, M. B. Sinclair, I. Brener, and F. Capolino, "Electrodynamic modeling of strong coupling between a metasurface and intersubband transitions in quantum wells," Phys. Rev. B **89**(16), 165133 (2014).
15. A. Benz, S. Campione, J. F. Klem, M. B. Sinclair, and I. Brener, "Control of strong light-matter coupling using the capacitance of metamaterial nanocavities," Nano Lett. **15**(3), 1959–1966 (2015).
16. R. Adato, A. A. Yanik, J. J. Amsden, D. L. Kaplan, F. G. Omenetto, M. K. Hong, S. Erramilli, and H. Altug, "Ultra-sensitive vibrational spectroscopy of protein monolayers with plasmonic nanoantenna arrays," Proc. Natl. Acad. Sci. U. S. A. **106**(46), 19227–19232 (2009).
17. A. V. Kabashin, P. Evans, S. Pastkovsky, W. Hendren, G. A. Wurtz, R. Atkinson, R. Pollard, V. A. Podolskiy, and A. V. Zayats, "Plasmonic nanorod metamaterials for biosensing," Nat. Mater. **8**(11), 867–871 (2009).
18. F. Cheng, X. Yang, and J. Gao, "Ultrasensitive detection and characterization of molecules with infrared plasmonic metamaterials," Sci. Rep. **5**(1), 14327 (2015).
19. W. Wan, X. Yang, and J. Gao, "Strong coupling between mid-infrared localized plasmons and phonons," Opt. Express **24**(11), 12367–12374 (2016).
20. L. Chen, D. G. Liao, X. G. Guo, J. Y. Zhao, Y. M. Zhu, and S. L. Zhuang, "Terahertz time-domain spectroscopy and micro-cavity components for probing samples: a review," Frontiers Inf. Technol. Electronic. Eng. **20**(5), 591–607 (2019).
21. E. Hendry, T. Carpy, J. Johnston, M. Popland, R. V. Mikhaylovskiy, A. J. Lapthorn, S. M. Kelly, L. D. Barron, N. Gadegaard, and M. Kadodwala, "Ultrasensitive detection and characterization of biomolecules using superchiral fields," Nat. Nanotechnol. **5**(11), 783–787 (2010).
22. Y. Zhao, A. N. Askarpour, L. Sun, J. Shi, X. Li, and A. Alù, "Chirality detection of enantiomers using twisted optical metamaterials," Nat. Commun. **8**(1), 14180 (2017).
23. J. Kischkat, S. Peters, B. Gruska, M. Semtsiv, M. Chashnikova, M. Klinkmüller, O. Fedosenko, S. Machulik, A. Aleksandrova, G. Monastyrskyi, Y. Flores, and W. Ted Masselink, "Mid-infrared optical properties of thin films of aluminum oxide, titanium dioxide, silicon dioxide, aluminum nitride, and silicon nitride," Appl. Opt. **51**(28), 6789–6798 (2012).
24. A. D. Rakić, A. B. Djurišić, J. M. Elazar, and M. L. Majewski, "Optical properties of metallic films for vertical-cavity optoelectronic devices," Appl. Opt. **37**(22), 5271–5283 (1998).
25. G. Duan, C. Zhang, A. Li, X. Yang, L. Lu, and X. Wang, "Preparation and Characterization of Mesoporous Zirconia Made by Using a Poly (methyl methacrylate) Template," Nanoscale Res. Lett. **3**(3), 118–122 (2008).
26. A. E. Cetin, S. Korkmaz, H. Durmaz, E. Aslan, S. Kaya, R. Paiella, and M. Turkmen, "Quantification of Multiple Molecular Fingerprints by Dual-Resonant Perfect Absorber," Adv. Opt. Mater. **4**(8), 1274–1280 (2016).
27. A. Naweed, G. Farca, S. I. Shopova, and A. T. Rosenberger, "Induced transparency and absorption in coupled whispering-gallery microresonators," Phys. Rev. A **71**(4), 043804 (2005).
28. R. Taubert, M. Hentschel, J. Kästel, and H. Giessen, "Classical Analog of Electromagnetically Induced Absorption in Plasmonics," Nano Lett. **12**(3), 1367–1371 (2012).
29. N. T. Fofang, T.-H. Park, O. Neumann, N. A. Mirin, P. Nordlander, and N. J. Halas, "Plexcitonic nanoparticles: plasmon− exciton coupling in nanoshell− J-aggregate complexes," Nano Lett. **8**(10), 3481–3487 (2008).
30. S. Savasta, R. Saija, A. Ridolfo, O. Di Stefano, P. Denti, and F. Borghese, "Nanopolaritons: vacuum Rabi splitting with a single quantum dot in the center of a dimer nanoantenna," ACS Nano **4**(11), 6369–6376 (2010).
31. X. Liu, T. Galfsky, Z. Sun, F. Xia, E.-C. Lin, Y.-H. Lee, S. Kéna-Cohen, and V. M. Menon, "Strong light–matter coupling in two-dimensional atomic crystals," Nat. Photonics **9**(1), 30–34 (2015).
32. E.-M. Roller, C. Argyropoulos, A. Högele, T. Liedl, and M. Pilo-Pais, "Plasmon–exciton coupling using DNA templates," Nano Lett. **16**(9), 5962–5966 (2016).
33. D. J. Shelton, I. Brener, J. C. Ginn, M. B. Sinclair, D. W. Peters, K. R. Coffey, and G. D. Boreman, "Strong Coupling between Nanoscale Metamaterials and Phonons," Nano Lett. **11**(5), 2104–2108 (2011).
34. X. Zhang, D. Wu, C. Sun, and X. Zhang, "Artificial phonon-plasmon polariton at the interface of piezoelectric metamaterials and semiconductors," Phys. Rev. B **76**(8), 085318 (2007).
35. B. Lahiri, S. G. McMeekin, R. M. De La Rue, and N. P. Johnson, "Enhanced Fano resonance of organic material films deposited on arrays of asymmetric split-ring resonators (A-SRRs)," Opt. Express **21**(8), 9343–9352 (2013).
36. L. S. Jung, C. T. Campbell, T. M. Chinowsky, M. N. Mar, and S. S. Yee, "Quantitative Interpretation of the Response of Surface Plasmon Resonance Sensors to Adsorbed Films," Langmuir **14**(19), 5636–5648 (1998).
37. B. Liedberg, I. Lundström, and E. Stenberg, "Principles of biosensing with an extended coupling matrix and surface plasmon resonance," Sens. Actuators, B **11**(1-3), 63–72 (1993).